*Limnol. Oceanogr.*, 53(5, part 2), 2008, 2151–2168


# Glider surveillance of physics and biology in the southern California Current System

*Russ E. Davis,*[1] *Mark D. Ohman, Daniel L. Rudnick, and Jeff T. Sherman*
Scripps Institution of Oceanography, La Jolla, California 92093

*Benjamin Hodges*
Woods Hole Oceanographic Institution, Woods Hole, Massachusetts 02543

*Abstract*

Since 2005, *Spray* underwater gliders have been used to sample sections across the southern California Current System (CCS). Properties measured are depth-averaged velocity and profiles of temperature, salinity, Acoustic Doppler Profiler shear, chlorophyll *a* fluorescence, and 750-kHz acoustic backscatter. Although slow and carrying a relatively small sensor suite, gliders observed multiple 350–700-km sections that reveal details of known elements of the CCS circulation like the California Current and Undercurrent as well as a previously undescribed undercurrent 100–200 km offshore. The long time series with high spatial resolution disclose the close link between fronts in physical and biological variables, both the main pycnocline front and secondary weaker but sharp fronts farther offshore. These fronts appear to organize chlorophyll and acoustic backscatter fields, particularly during spring. Much of the patchiness of chlorophyll is associated with vertical displacements of fields that are much smoother within potential density surfaces. The horizontal structure of both chlorophyll and spice (the dynamically passive variable formed from temperature and salinity) appear to be formed by mesoscale stirring.

The California Current System (CCS) is a highly productive eastern boundary current supported by coastal upwelling and eddy activity. The CCS includes the California Current carrying cold, fresh, nutrient-laden waters equatorward (Hickey 1979; Lynn and Simpson 1987); warm, salty poleward flow in the California Undercurrent (Lynn and Simpson 1990; Collins et al. 2000); well-defined upwelling jets north of Pt. Conception; and vigorous fields of eddies, fronts, and squirts (Davis 1985; Kelly et al. 1998; Chereskin et al. 2000). The southern CCS experiences weaker wind forcing and strong bathymetric influences from the Channel Islands and Pt. Arguello and Pt. Conception and is frequently dominated by the Southern California Eddy, which includes poleward flow along the coast. While the southern part of the CCS has less primary productivity than the more strongly wind-forced area to the north, it is the spawning grounds (Saunders and McFarlane 1997; Checkley et al. 2000) for many upper-trophic-level species (sardines, hake, and squid having the greatest economic import), and, because survival in the larval stage is critical to recruitment, processes in the southern CCS have consequences throughout the CCS ecosystem. Physical climate variability on seasonal to interannual time scales (Chelton and Davis 1982), in the form of ENSO (Ramp et al. 1997; Lynn and Bograd 2002), lower-frequency variability including the Pacific Decadal Oscillation (Mantua et al. 1997), and apparently secular changes of stratification (Roemmich and McGowan 1995; Kim and Miller 2007; Lavaniegos and Ohman 2007) all significantly alter the CCS ecosystem.

The California Cooperative Oceanic Fisheries Investigations (CalCOFI) has documented large-scale changes of the physical state of the southern CCS for 58 years and the changes in plankton, fish eggs, and larvae that accompany these changes (Ohman and Venrick 2003). While patterns of physical and biological variability have been recognized and the association of biological and physical variability has been enunciated, the mechanisms producing and linking the patterns remain largely unknown: large-scale variability of alongshore currents can change the transport of biota and nutrients, stratification and upwelling variability modulate nutrient supply to the food web base, and changes of temperature affect behavior and species success. On the mesoscale, eddies, fronts, and cross-shelf squirts produce unique pelagic habitats by bringing distinct water types in close proximity, making these mesoscale features central to the ecosystem and its variability (Hayward and Mantyla 1990; Logerwell and Smith 2001).

Development of the long-duration Autonomous Underwater Vehicles called underwater gliders (Davis et al. 2002; Rudnick et al. 2004) offers the possibility of sustaining long-term, high-resolution, broad-area observations of important coastal processes. This paper describes the start of an effort to use gliders to resolve the mechanisms underlying lower-frequency variations in the pelagic ecosystem of the southern CCS. Because gliders are slow

[1] Corresponding author (rdavis@ucsd.edu).

*Acknowledgments*

This work was supported by the Gordon and Betty Moore Foundation, the National Oceanic and Atmospheric Agency's Ocean Climate Observations program, the National Science Foundation's California Current Ecosystem Long Term Ecological Research program, and the California Coastal Conservancy. We thank Brent Jones, Jim Dufour, David Black, and Kyle Grindley for preparing and deploying the *Spray* gliders; Ben Maurer and Jesse Powell for calibrating Acoustic Doppler Profilers and fluorometers; and Mati Kahru for processing the Moderate Resolution Imaging Spectroradiometer (MODIS)-Aqua satellite imagery (furnished by the National Aeronautics and Space Agency). Two anonymous reviewers were very helpful.

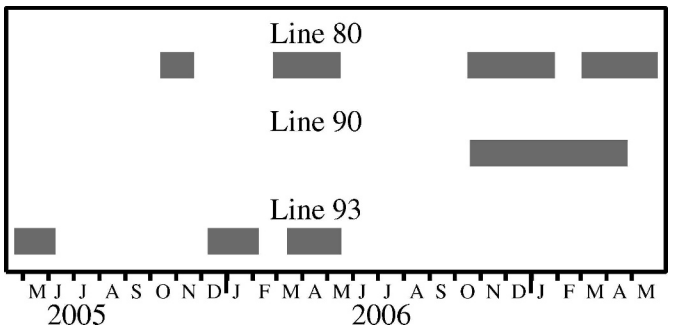


Fig. 1. Time periods of the glider measurements discussed in this paper. Figure 2 shows their locations.

moving, synoptic sections are impossible, and because gliders can support only the simplest low-power sensors, they provide only indicators of the ecosystem. But the ability to support numerous sustained observations compensates for these limitations. A glider can measure over relatively extended periods of time (ca. 100 d with our present payload) and space (ca. 2500 km) while measuring vertical structure of the water column on horizontal scales of a few kilometers. Eddies, fronts, coastal filaments, and other mesoscale features of biological significance whose surface expressions are sensed by satellites can be observed throughout the water column. Immediate telemetry of data and bidirectional communications allow us to adapt sampling to unexpected phenomena. Because glider operating costs are low, glider sampling can be frequent enough to resolve key processes that alter the pelagic ecosystem (e.g., the spring transition and the onset and decay of El Niño).

Our glider-based observations in the CCS began with engineering development runs on CalCOFI Line 93, which starts near La Jolla and, like all CalCOFI lines, extends WSW, roughly perpendicular to the inshore California Undercurrent and the California Current. With an expanded sensor suite, operations were carried to Line 80, which extends WSW from the major upwelling center near Pt. Conception (cf. Smith et al. 1986). Early time series have large gaps because of glider availability. In the autumn of 2006, we established an additional glider section along Line 90, the most regularly sampled line in the CalCOFI region, which runs WSW from Dana Point. All glider lines begin just outside the kelp zone and extend across the Southern California Bight into highly stratified waters offshore, crossing major gradients in hydrographic and plankton properties. The timing of the measurements discussed here is shown in Fig. 1, and locations are in Fig. 2; today, Lines 80 and 90 are being observed continuously.

The largest temporal variability is associated with the seasonal cycle. As this cycle is established, the variations associated with interannual climate variability should emerge, but this will take years of sustained observations. In the meantime, the most vigorous nonseasonal variations are associated with mesoscale variability in fronts and eddies, and a theme of this paper is trying to provide a statistical description of the processes, physical and biological, occurring on this scale.

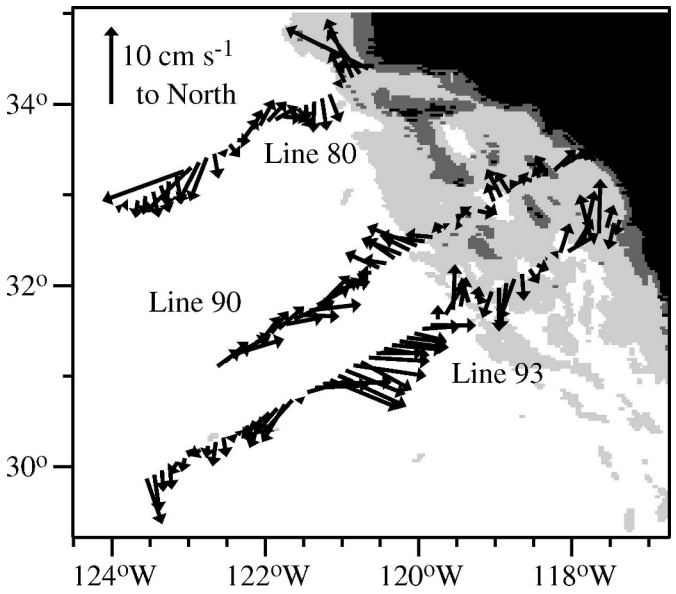


Fig. 2. Overall mean of depth-averaged velocity (0–500 m or the bottom) from the cruises depicted in Fig. 1. Bathymetric shading breaks at 0-, 200-, and 1500-m depth.

Gliders are used to support ship-based research of the California Current Ecosystem Long Term Ecological Research site in two ways. In both cases, we operate gliders in one location while the research vessel is operating in another. In one application, we use advance glider mapping of a region to identify fronts and other features and, thus, locate subsequent shipboard stations in appropriate places where hydrographic and plankton properties are known in advance. In a second application, *Spray* is used in conjunction with a quasi-Lagrangian satellite-located drifter to track the temporal evolution of a water parcel. Unlike Lagrangian drifters, which measure at a single point, the glider maps the characteristics around the drifter. While the ship is otherwise occupied, the glider is used to understand the characteristics of the water parcel and establish its three-dimensional structure and entrained plankton populations as it translates through space.

## Methods

*Spray* (Sherman et al. 2001) is a 50-kg, 2-m-long underwater glider capable of operating to below 1000-m depth for durations of 4 months. As it moves forward at speeds near 25 km $d^{-1}$, the glider cycles vertically at ascent and descent angles of about 18° from the horizontal. *Spray* is piloted by commands from shore and relays data to shore using Iridium; it records more data internally. The angle of attack between the glider axis and relative velocity is well enough known that the glider's velocity through the water can be found from measured vertical velocity under the assumption of weak vertical flow. Comparing distance traveled through the water with surface GPS fixes measures the depth-averaged (over the glider's operating range) current.

In the southern CCS, *Spray* is typically deployed and recovered from a small boat not far outside the kelp zone.

It glides along a sawtooth profile to the chosen section and is directed offshore, diving to the shallower of the bottom or typical 500-m depth. Piloting involves a sequence of waypoints and one of the following steering modes: maintain a prescribed heading, head toward the next waypoint, head toward the next waypoint correcting for set and drift of the depth-averaged current predicted from previous measurements, and maintain a prescribed heading relative to the measured current. The latter mode is most helpful crossing strong currents. We often do not send a new command to the glider for days, but they can be sent at each surfacing. A typical speed of advance is 25 km $d^{-1}$; a dive to 500 m takes about 3 h, advances position about 3 km, and ends in a 7–10-min on-surface period where communication and navigation are accomplished and surface drift estimated.

To observe physical structure and provide indicators of biological properties, *Spray* was fitted with a Sea-Bird 41CP conductivity-temperature-depth (CTD) sensor, a Sontek 750-kHz Acoustic Doppler Profiler (ADP), and a Seapoint chlorophyll *a* fluorometer. The ADP measures shear over about 25 m below the glider and doubles as an altimeter for bottom avoidance. Depth-averaged velocity is used to reference geostrophic shear and velocity profiles obtained by integrating ADP shears. The CTD provides measurements of density for dynamics and temperature vs. salinity as indicators of differing water types. Chlorophyll *a* (Chl *a*) fluorescence is our indicator of phytoplankton biomass, and ADP backscatter strength is our indicator of zooplankton biomass (primarily in the 2–10-mm size range due to the steepness of the size spectrum of plankton). To conserve energy and get the lowest sensor noise levels, sensors are operated only during ascent, except for one ADP beam used as an altimeter.

Early experience showed that conventional optical sensors were often biofouled into inoperability in a few weeks of operation in the CCS. At the same time, Sea-Bird suggested that calibrations developed to compensate for thermal lags (Johnson et al. 2007) in an unpumped CTD would always be uncertain on gliders because of variations in the angle and speed of the flow past the CTD. These two problems are solved simultaneously by using the 41CP's low-power water pump during sampling and plumbing optics into the exhaust stream of the CTD. This allows the CTD entrance to be fashioned to discourage particles from entering the water system while toxic pellets raise the concentration of poison throughout the system, particularly when the pump is not running.

Some calibration or intercruise comparison is required to verify that antifouling is effective and to permit comparison between cruises and vehicles. Inferring in situ chlorophyll or phytoplankton concentration from a fluorometer depends logically on (1) linking instrument output (volts) to optics (excitation intensity and reception sensitivity) so that fluorescence can be accurately measured and (2) relating variations of fluorescence to phytoplankton physiology and biomass. Both calibration steps are required before fluorescence time series can be fully interpreted. While the complex fluorescence vs. biomass relation is yet to be clarified, we provide an accurate characterization of the observed fluorescence itself, fully realizing that this does not directly relate our measurements to phytoplankton biomass. In the laboratory, before and after each glider mission, we measured the optical response of the fluorometer to serial dilutions of pure Chl *a* (Sigma C6144) in 90% acetone contained in a cuvette with an 11-mm light path. We have detected only small changes in fluorometer response (a mean change of 9% with a 95% confidence limit of 8%) after up to 97 d at sea, reflecting long-term stability and negligible effects of biofouling. To allow our fluorescence measurements to be compared with those made at other times and places, we report them in dissolved Chl *a* fluorescence equivalents (DCFE). A DCFE is defined as the fluorescence signal produced by a 10 $\mu$g $L^{-1}$ solution of pure Chl *a* in 90% acetone. For in vivo fluorescence of naturally occurring phytoplankton in seawater, measured by a Seapoint fluorometer with excitation centered at 470 nm and emission at 685 nm (manufacturer's specifications), one DCFE corresponds very approximately to 1 $\mu$g $L^{-1}$ phytoplankton Chl *a*. We encourage reporting fluorescence in DCFEs (or some equivalent absolute measure of fluorescence) so that the relation of biomass to absolute fluorescence can be developed.

Comparability of acoustic backscatter measurements is also needed to observe long-term changes. This depends on calibrating the ADP as an acoustic instrument and is improved when there is a relation between zooplankton biomass and scattering cross section. Prior to and following each glider mission, we calibrate each of the three beams of the ADP in an acoustic test tank using as an acoustic reflector a suspended tungsten-carbide reference sphere. This procedure amounts to mapping out the directional pattern for each beam. In the early missions reported here, our procedure was accurate enough only to show that each ADP was stable between successive missions to the order of 2 dB, so we report acoustic backscatter (ABS) in dB relative to an arbitrary reference that does not change much between missions.

## Large-scale circulation

The CCS is variable seasonally and is home to energetic mesoscale eddies. At the same time, there are persistent and recurrent features including the California Current, the poleward California Undercurrent frequently centered near the upper continental slope, seasonal poleward flow over the shelf, shallow nearshore equatorward currents associated with upwelling, and the Southern California Eddy, a cyclonic eddy with a low centered about 100 km offshore over the Channel Islands. While the CCS glider time series are too short and too nonuniform seasonally to construct mean fields that are free from eddy effects, it is interesting to see what these first sustained high-resolution observations of the Southern California Bight describe in the aggregate.

The overall mean of observed depth-averaged velocity (to the shallower of 500 m or the bottom) is shown in Fig. 2. Most obvious in this plot is the absence of the coherent and smooth structure that is typical of near-surface circulation

maps drawn from quarterly CalCOFI hydrographic surveys (cf. Chereskin and Trunnell 1996). The added structure comes partly from incompletely averaged temporal variability, partly from small-scale features not seen in low-resolution data, and partly from features in absolute velocity that are not found in dynamic height. Substantial contribution from temporal variability is likely, but the question of the impact of swirls and filaments in the mean CCS circulation has remained unanswered since it was raised by Hickey (1979). In Fig. 2, nearshore poleward flow is evident on Lines 80 and 93; similar averages over different time periods show that this is stronger in autumn and winter and also appears on Line 90 in those seasons. Equally strong zones of poleward depth-averaged flow found offshore are discussed later.

Coupling velocity data, like those in Fig. 2, with geostrophic shear computed from the glider CTD provides sections of absolute velocity in which the depth-averaged geostrophic velocity is referenced by the measured depth-averaged velocity. Figure 3 shows the mean flow across Lines 80 and 93 based on average density sections using all our CTD data and the mean depth-averaged flow shown in Fig. 2. By referencing geostrophic shear to measured transport, we have neglected Ekman transport through the sections, which seems justifiable because the annual average wind velocity is largely normal to the CalCOFI sections.

Both sections in Fig. 3 show the flow below 200 m to be frequently poleward with a concentrated poleward undercurrent over the continental slope. More surprising is the poleward flow found around 200 km offshore. These two poleward flows, found in both sections, appear as equatorward geostrophic flows when referenced to no motion at 500 m or the bottom and are identified as poleward flows only when referenced by the glider measured velocities. The equatorward flows found between and offshore of these poleward flows are presumably parts of the California Current, which is seen mainly above 200 m depth.

Because of the shortness of the available record, the mean velocity in Fig. 3 is subject to significant sampling error. Nevertheless, the strength of the main features, as well as their appearance on both well-measured sections, suggests they are elements of the general circulation. Presumably the poleward flows are the southern California Bight analogues of what Collins et al. (2000) call the Inshore Countercurrent and the California Undercurrent, both of which are well marked by water properties and occasionally observed directly. Chereskin and Trunnel (1996) reference southern California Bight geostrophic shear with ADCP currents for October 1993 and find a coherent offshore poleward flow at 500-m depth that crosses Line 80 about 100 km offshore and crosses Lines 90 and 93 about 200 km out. Assuming the continuity and persistence that our results suggest, both these currents have important implications for how larvae and other plankton disperse along the coast. As our results and those from Chereskin and Trunnell (1996) show, knowing the true circulation pattern of the CCS will require absolute velocity measurements repeated many times.

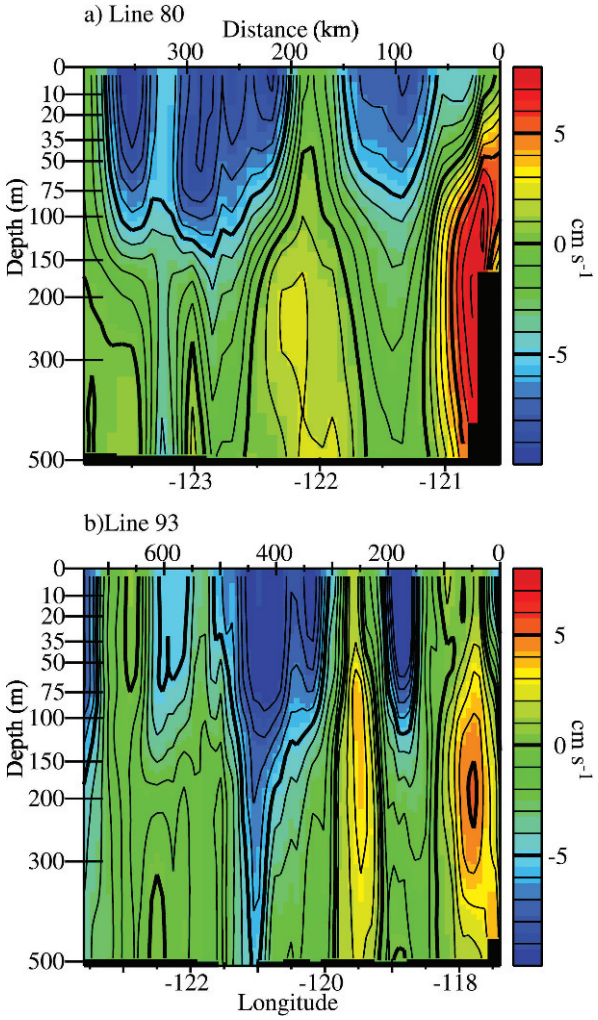


Fig. 3. Mean absolute poleward geostrophic flow referenced to measured depth-averaged velocity plotted against longitude and distance offshore. (a) Line 80, (b) Line 93. The California Undercurrent, evident over the slope, and the major poleward undercurrent found 200–250 km offshore are both seen only after referencing to measured depth-integrated velocities. The ~200-km-wide current above 200 m is a filament of the California Current.

## Synoptic structures

Here we show features disclosed by the unusual combination of high-resolution data and the long time series that gliders make possible.

*Anticyclonic eddy off Pt. Conception*—In October–November 2005, we detected a persistent anticyclonic eddy on CalCOFI Line 80 offshore of Pt. Conception (Fig. 4a). Because the steering mode did not compensate for currents, the glider was displaced off track in relatively rapid flows to the SSW on the outbound leg and to the NNE on the inbound leg. The vertically averaged (0–400 m) water column velocity was 20–25 cm $s^{-1}$ in the eddy and considerably slower to both the NE and the SW (Fig. 4a). Satellite-derived Chl *a* fields show the clockwise sense of

the eddy, with the edges delimited by chlorophyll fronts and isopycnal surfaces below 150-m depth (Fig. 5) depressed in the eddy core, consistent with a geostrophic anticyclonic eddy.

The subsurface structure of the eddy is dominated by fronts in seawater density, Chl *a* fluorescence, and acoustic backscatter that characterize the eddy boundaries (Fig. 5). Both fronts were boundaries between fresher, warmer surface waters offshore and saltier, colder, and denser water nearer the coast. Phytoplankton concentrations and vertical distributions also changed abruptly near the fronts. Phytoplankton pigment concentrations were markedly higher inshore of the eddy, while at the offshore front the near-surface Chl *a* peak decreased abruptly, forming a deep chlorophyll maximum (DCM) at 20–35-m depth that continued to deepen with distance offshore. These frontal transitions often occurred between two dives (i.e., over 2–3 km). Acoustic backscatter at 750 kHz also changed at the eddy frontal boundaries. At all depths, backscatter was locally enhanced near the fronts, while the broad-scale backscatter level decreased going offshore at both fronts. These signatures are clouded by the well-defined periodic pattern of a daytime backscatter maximum between 200- and 300-m depth and a nighttime maximum between 0- and 50-m depth (Fig. 5), corresponding to diel vertical migration by zooplankton and micronekton.

A noteworthy feature detected on the inbound glider section but not the outbound is a packet of internal waves seen just inshore of the eddy in Fig. 5. The height of these waves was 20–25 m at 50-m depth and about 50–55 m at a depth of 200 m, and their period was approximately 12 h, presumably a semidiurnal tidal period. These waves appeared at the time of the semidiurnal spring tide.

The next glider on Line 80 headed offshore at Pt. Conception in early March 2006, about 4 months after the cruise shown in Figs. 4 and 5. On the first outbound and return legs, which ended at the start of April, an anticyclonic eddy was found at the same location as the previously observed eddy. The density, chlorophyll, and acoustic backscatter signatures were also similar (*see* Fig. 6). On the second offshore section in April 2006, we planned to map the eddy, but it was gone and has not been seen again for a year. Whether the eddy persisted for 6 months or recurred, the existence of this feature raises questions about the roles that eddies play in the seasonal mean circulation and in retaining organisms in a unique habitat for months. The impact of this eddy on the mean flow in Figs. 2 and 3 is significant. If a second average is made by deleting the two missions in which it was found and replacing them with two from 2007, the correlation of the two time-averaged offshore profiles of depth-averaged velocity is only 0.65, and it is clear that much of the difference between the averages is the signature of the persistent eddy seen in Figs. 4 and 5. Only continued sampling will determine the mean velocity section and whether this feature is unique.

*Seasonal variation of cross-shore structure*—In 2006, a glider on Line 80 completed four sections between 01 March and 11 May (the spring sequence) and another four between 20 October and 05 January 2007 (the fall sequence). The cross-shore sections extended 300–350 km offshore and to 500-m depth. These are shown in Fig. 6 (spring) and Fig. 7 (fall), where the most obvious changes occur on the large scale. The slope of the main pycnocline ($\sigma_\theta \approx 25.5$) increases during the spring sequence, particularly near the coast, from March to early May in response to increasing upwelling-favorable seasonal wind evolution all along the coast (Lynn et al. 2003); the coastal upwelling index (http://www.pfeg.noaa.gov/PFEL/products/modeled/indices/PFELindices.html) for 33–39°N indicates 2006 to have had a normal if somewhat attenuated seasonal upwelling cycle. In autumn and into early winter, the main pycnocline flattens as geostrophic shear diminishes seasonally (Lynn and Simpson 1987), although the nearshore remains slightly denser than offshore. The near-surface warm, fresh ($S < 33.5$) layer of northern origin is fresher in spring than fall, when the freshest water is often found near the base of the mixed layer at depths of 50–80 m. In spring, the main pycnocline and main halocline reach the surface at nearly the same location, near the inshore end of the sections. In fall, these surfaces do not generally outcrop. In spring, Chl *a* is focused within 100 km of shore while offshore surface waters have little Chl *a* and overlie a DCM near the depth of the main pycnocline. In fall, particularly late in the sequence, Chl *a* generally fills the mixed layer and is fairly uniform along the sections. Acoustic backscatter exhibits characteristics of diel migration and has enhanced intensity in the surface layer within 100 km of the coast. Some of the fall near-surface maxima in acoustic backscatter are likely due to wind mixing and entrainment of air bubbles rather than scattering off organisms.

A closer look, made possible by the long series of high-resolution measurements, emphasizes the importance of frontal features within the upper layer (Fig 6. for spring and Fig. 7 for fall). During spring, there are, in addition to the main pycnocline–halocline front, other sharp but low-contrast density, salinity, and often Chl *a* fronts in the upper layer. The secondary fronts in salinity and temperature frequently coincide in both seasons. They move horizontally and are nearer shore and less variable in spring. The springtime fronts are tightly linked to Chl *a* and acoustic backscatter. Each secondary front marked in Fig. 6 coincides with a substantial change in Chl *a*, most separating an inshore side where Chl *a* is elevated and surface intensified from an offshore side where surface Chl *a* declines abruptly and a DCM forms. The springtime acoustic records also show a frontal transition in the intensity of backscatter. Both near the surface and in deeper layers, backscatter diminishes markedly offshore of the secondary density front while it increases inshore of the front.

In the fall sequence (Fig. 7), all variables have less large-scale horizontal structure and weaker stratification than in spring. Perhaps as a consequence, fronts in all variables are weaker and less predictable. Unlike spring, Chl *a* patterns are indistinct and the highest Chl *a* concentrations are found offshore; these higher-chlorophyll regions are often associated with weak and variable temperature and salinity structure in the mixed layer. Acoustic backscatter, on the other hand, is if anything more concentrated in the inner

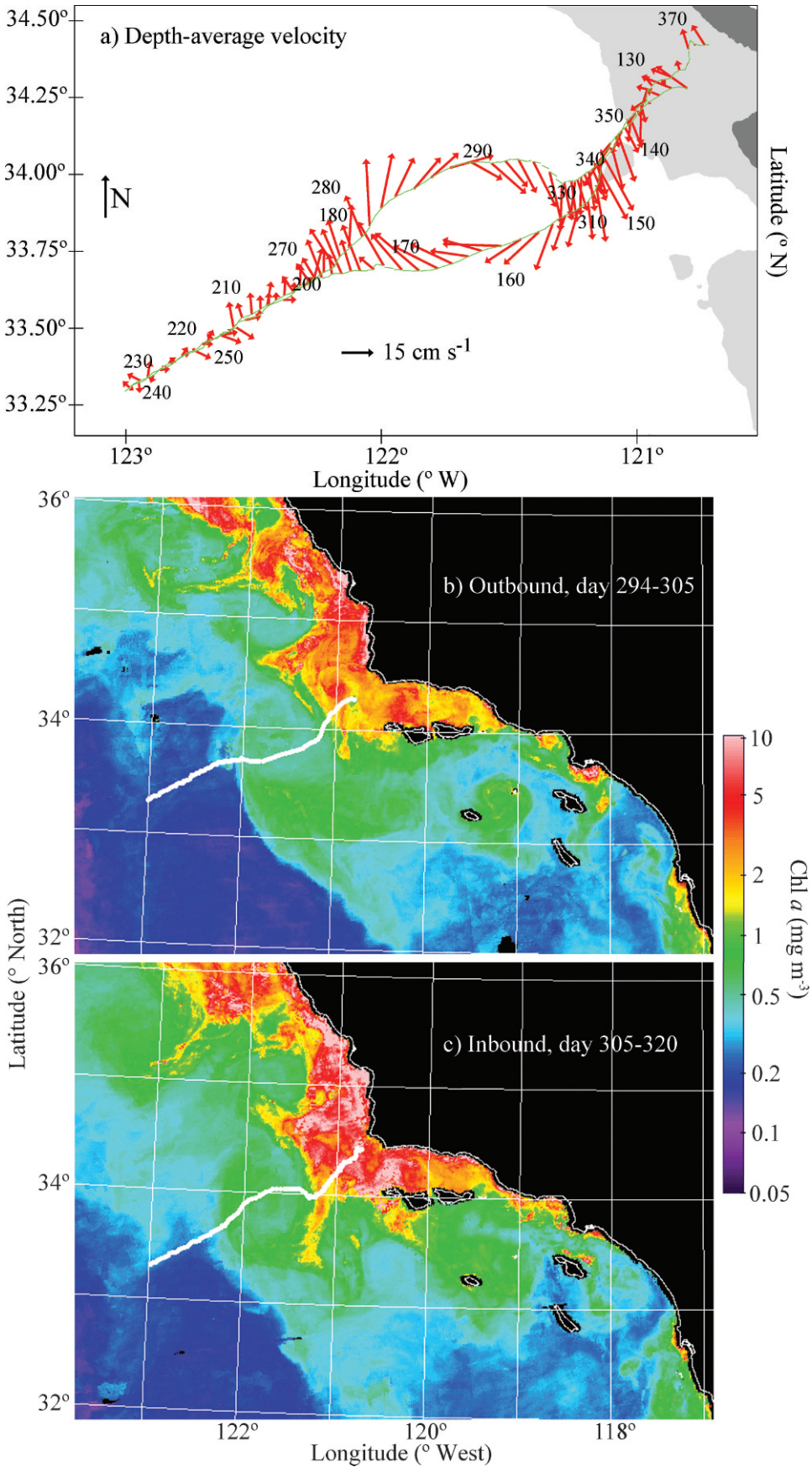
a) Depth-average velocity
34.50°
34.25°
34.00°
33.75°
33.50°
33.25°
N
15 cm s-1
370
130
350
140
290
340
280
330
180
310
150
270
170
160
210
200
220
250
230
240
123°
122°
121°
Longitude (° W)
Latitude (° N)
b) Outbound, day 294-305
c) Inbound, day 305-320
36°
34°
32°
122°
120°
118°
Longitude (° West)
Latitude (° North)
10
5
2
1
0.5
0.2
0.1
0.05
Chl a (mg m-3)

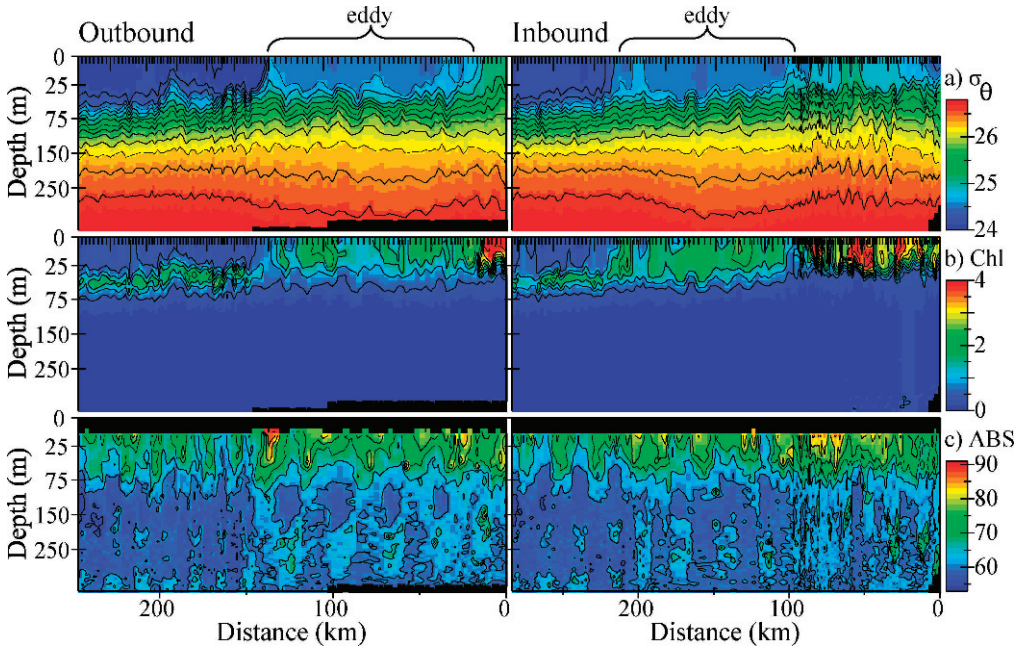


Fig. 5. Glider sections along Line 80 outbound (21 Oct–01 Nov 2005) and inbound (01–16 Nov 2005) showing a persistent anticyclonic eddy. Panels show (a) potential density, (b) Chl *a* fluorescence (DCEF; *see* "Methods"), and (c) acoustic backscatter (uncalibrated dB).

100 km, where local maxima continue to be associated with physical gradients in both the mixed layer and the deeper water. These seasonal distributions imply greater uniformity of phytoplankton in winter than in spring while zooplankton remain concentrated nearshore. Such a seasonal difference in spatial patterning of the plankton community should have consequences for predator–prey interactions in the ocean.

## Physical scales

Analysis of high-resolution observations (1) reveals scales of variability needed to assess the resolving power of observational arrays and (2) describes characteristic patterns of temporal-spatial change and covariation that may indicate underlying processes. With only one slow-moving glider operating in a region at a time, we cannot separate space and time scales as can be done with data from moorings or fast-moving platforms. As with Lagrangian data, space and time scales from a single glider are linked, although gliders are not constrained to follow fluid motion. (Glider arrays can resolve combinations of space and time variability.) Here we present some useful analyses made possible by long series from gliders with low operating speeds.

*Velocity*—Horizontal and vertical scales are often described with correlation distances and times or with the empirical orthogonal functions deduced from time- and space-separated correlations. To avoid the difficulty of estimating mean fields and variances from our short data set, we use the structure function (the mean-square difference between observations at two positions and times) and average over selected seasons and all positions. The structure function of $T(x, t)$ is

$$Q(x,t) = \langle [T(r + x, s + t) - T(r, s)]^2 \rangle_{r,s},$$

where $< >_{r,s}$ denotes the average over positions $r$ and times $s$. This was introduced by Kolmogorov (1941) to provide a statistical description of small-scale structures that did not require measuring mean values and variances that in environments like the ocean depend on the largest scales of variability. If the mean and variance, $<T>$ and $<T'^2>$ were known, the time- and space-lagged correlation would be

$$r(x,t) = 1 - \frac{1}{2} Q(x,t) \Big/ \langle T'^2 \rangle,$$

so $Q$ provides much the same information as the correlation without requiring that large-scale and low-frequency variability be well characterized so that the mean and variance are known. The scale over which the correlation approaches zero equals the scale over which $Q$ approaches twice the variance.

←

Fig. 4. (a) Depth-averaged 0–400-m velocity, (b) outbound track (solid white line) 21 Oct–01 Nov 2005, and (c) inbound path (solid white line) 1–16 Nov 2005. Glider paths are superimposed on a MODIS-Aqua-derived Chl *a* image composite for the corresponding dates (by M. Kahru, SIO). Note fronts marked by the yellow-to-green transition on the inshore and the green-to-blue transition on the offshore.

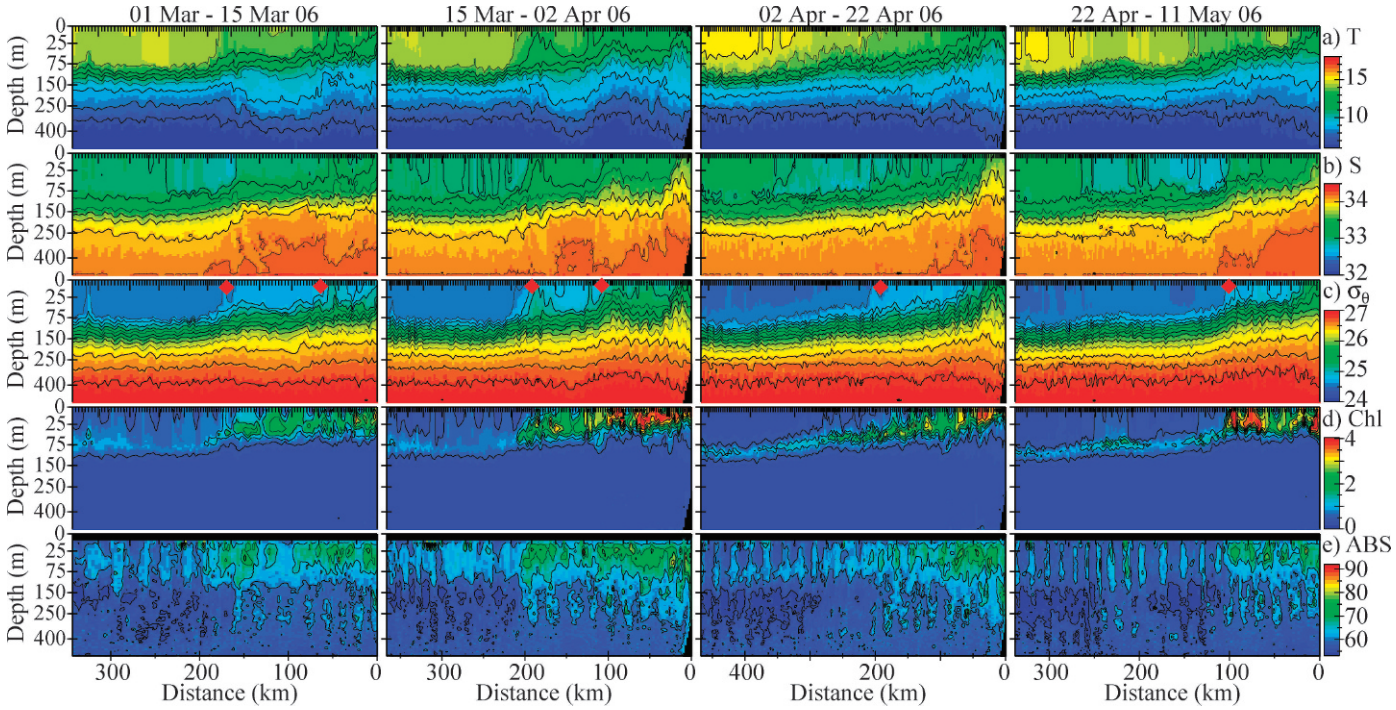


Fig. 6. Repeated glider sections on Line 80 from March to May 2006. Horizontal panels show (a) temperature (°C), (b) salinity, (c) potential density, (d) Chl *a* fluorescence (DCEF), and (e) 750-kHz acoustic backscatter (uncalibrated dB). Note the shallow frontal features (marked with red diamonds) that coincide in salinity, density, and Chl *a*. The fronts in the two sections from March 2006 mark the edges of an anticyclonic eddy at the same location as the one shown in Fig. 5.

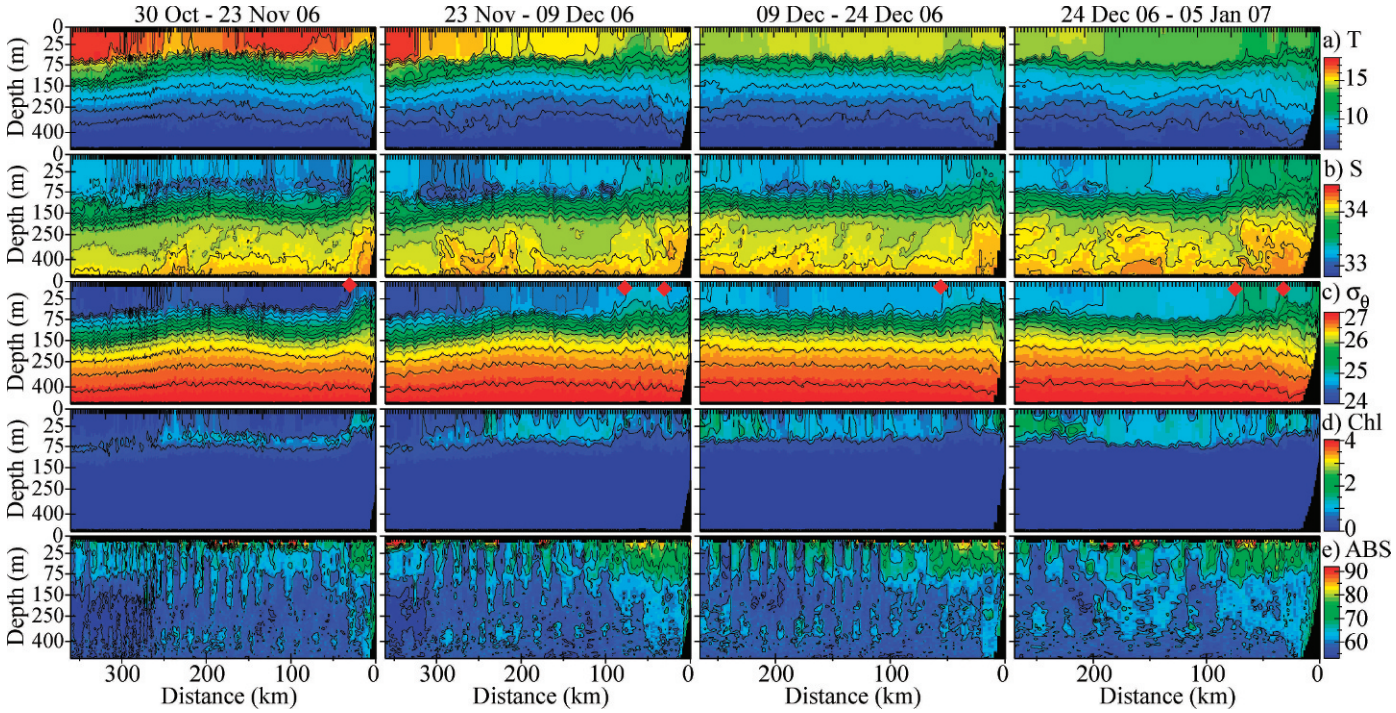


Fig. 7. Fall sequence of section from October 2006 to January 2007. Same format as Fig. 6.

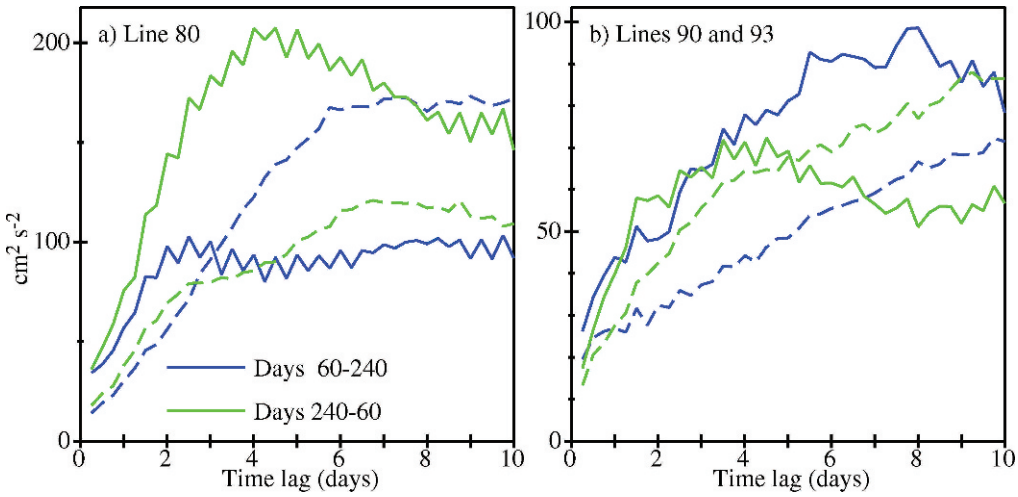


Fig. 8. Structure functions of depth-averaged alongshore (solid) and cross-shelf (dashed) velocity for the seasons March–August (blue) and September–February (green) using all data on CalCOFI (a) Line 80 and (b) Lines 90 and 93. Time bins are 6 h, making the clear alongshore tidal motion appear to be a sawtooth rather than a sinusoid.

Here data are taken along an individual glider's track and reported in terms of the time or distance between measurements. If glider velocity were a constant $q$, then the time-lagged structure function $Q(qt, t)$ could be converted to the spatially lagged function $Q(x, s/q)$ using the speed $q = 25$ km d$^{-1}$. Vehicle velocity variations caused by currents and course changes such as the ends of sections make this translation inexact.

Figure 8 shows the structure function of alongshore and cross-shelf (as defined by the CalCOFI lines) depth-averaged velocity as a function of time separation along Line 80 and along Lines 90 and 93. The general shapes of space-lagged functions are well approximated by equating 4-d lags with 100 km in Fig. 8. The velocity structure functions tend to rise to a peak or plateau at scales near 5 d (or 125 km). In the corresponding wave number or frequency spectra, a peak would translate into an energy concentration near that scale and a plateau to a cutoff at that scale. The velocity structures in Fig. 2 show ways that narrowband variability might be manifested. Figure 8 also shows strong tidal motions in the alongshore flow, particularly on Line 80; the implied amplitude is about 3 cm s$^{-1}$ on Line 80. Variations of glider speed and course make tides much less evident in the space-lagged structure functions.

Both time- and space-lagged structure functions of depth-averaged velocity show complex regional differences. On all scales, Line 80 is more energetic than are Lines 90 and 93 by nearly a factor of two, and Line 80 is more anisotropic. Line 80's anisotropy varies seasonally, with alongshore flow dominating in autumn–winter and cross-shelf variations stronger in spring–summer (except on the shortest scales less than 2 d or 50 km, which are approximately isotropic). To the south, anisotropy is mainly at larger scales (>5 d or 125 km) and is reversed seasonally from Line 80. Whether these characteristics are important clues to different mesoscale dynamics in the two regions (winds and upwelling are much stronger to the north) or are statistical quirks can be determined only with longer time series. It is, however, clear from Fig. 8 that in order to resolve velocity in the CCS, observations must not be separated by more than about 25 km.

*Salinity*—Salinity is a particularly useful water tracer for separating waters of northern and southern origin and as a marker for mesoscale features and fronts. The scales of salinity variability are shown in Fig. 9, where the structure function of $S$ is shown for two 6-month "seasons." In one plot, the mean-square salinity differences are between two points on level surfaces; in the other, the differences are between points on the same potential density surface. Figure 9 shows $S$ to vary nearly an order of magnitude more on levels than it does on density surfaces: much of the variability on a level surface results from heaving of the vertical stratification.

The shape of the $S$ structure function on levels is characteristic of a field dominated by very long scales (a trend in the data would produce a parabolic structure function). On levels, $S$ variability shows no obvious length scale because it is dominated by the largest accurately described scales around 200 km. The source of this variability is evident in the large-scale structure in Figs. 6 and 7. On many isopycnals, the variability seems to peak at the mesoscale, between 50 and 100 km. It is often said that the scale of temperature and salinity are longer on $\sigma_\theta$ surface than on levels. While the smaller variability of $S$ (and of $T$) on isopycnals makes their distribution smoother, the scales of variability in the southern California Bight are shorter on isopycnals than on levels. The seasonal cycle in Fig. 9 is noteworthy. Salinity on levels, which is dominated by the largest scales, is less variable in autumn–winter than in spring–summer, consistent with the smaller large-scale lateral gradients of salinity seen in fall (Fig. 7). On density surfaces, variability is substantially stronger in autumn, and the characteristic scale is better defined and smaller in fall than spring.

*Spice*—Potential temperature, $\theta$, and salinity, $S$, are the two tracers most frequently used to track flow in the ocean.

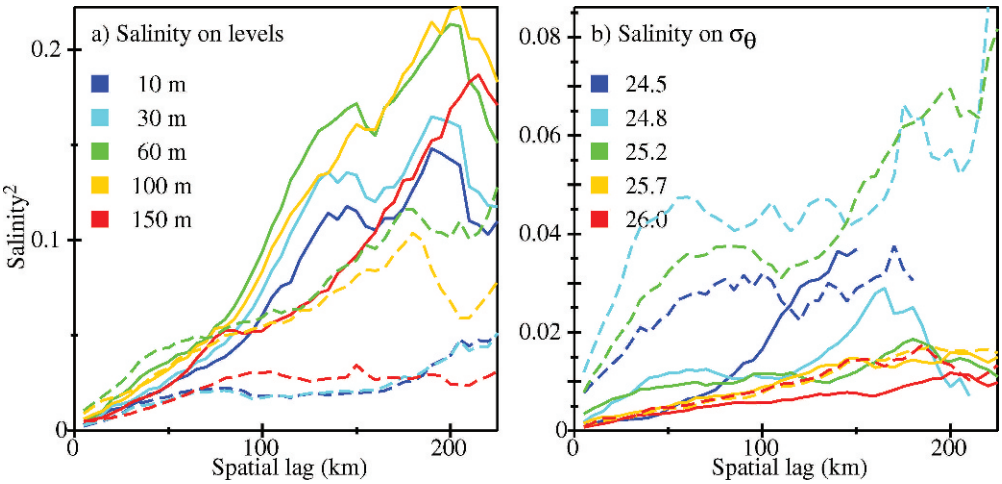


Fig. 9. Structure function of salinity variability on Line 80. (a) Mean square differences of $S$ on the 10-, 30-, 60-, 100-, and 150-m levels. (b) Structure functions of $S$ on the 24.8-, 25.2-, 25.7-, and 26.0 potential density surfaces. Results from March to July are solid lines, and those from August to February are dashed. Note that the more energetic season is opposite for levels and density surfaces and that the scales on levels are much larger than on density surfaces.

Both $\theta$ and $S$ are active in the sense that they affect the momentum balance through their effect on density. Veronis (1972) was the first to emphasize that a dynamically passive tracer that has no effect on the momentum balance is a useful indicator of flow history. A simple, approximately passive tracer is $\theta$ (or, equivalently, $S$) on a potential density surface. Munk (1981) called such tracers "spice," as water can vary from hot and salty to cold and fresh on a potential density surface. The concept has proven so useful that a variety of definitions of spice have been proposed (Veronis 1972; Jackett and McDougall 1985; Flament 2002). For simplicity, we examine $\theta$ and $S$ on $\sigma_\theta$ surfaces to avoid details of the differences between definitions and to minimize pressure effects; since all the measurements considered here are shallower than 500 m, $\sigma_\theta$ referenced to the surface is a reasonable neutral surface (McDougall 1987). The term "spice" is used in the following as a shorthand for $\theta$ or $S$ on a $\sigma_\theta$ surface. The structure function in Fig. 9b is thus one of spice. Spice is conservative, but in the mixed layer and near its base, mixing and radiation significantly affect spice, and at all depths diapycnal mixing keeps it from being precisely conserved.

The rich mesoscale flows in the California Current are often well described in spice. Closed eddies, whose edges can be very sharp, transport water of distant origins. Other fronts separating water of different characteristics, such as the front separating recently upwelled water from surface water, are often observed. These features and processes as revealed by spice are shown in Fig. 10. A common feature on Line 80 is the appearance of warm water of southern origin inshore and cool water of northern origin offshore. For example, in the spring of 2006 isopycnals heavier than about 25 kg m$^{-3}$ show this trend within 100 km of shore (Fig. 10a), particularly along the inclined front. Near 250 km, there is another sharp inclined spice front where the jump is from cool-fresh offshore to warm-salty onshore at 26 kg m$^{-3}$, but above that the spice change is of the opposite sign on isopycnals near the mixed-layer base. Such vertical stacking of spice gradients of opposite sense is observed in several other sections. How common these features are, their exact mechanism, and whether they are seasonally dependent awaits the collection of more glider data.

Another front, with warm-salty water on the inshore side, is apparent on Line 90 in the fall of 2006 at about 300 km offshore (Fig. 10b). Here, the spice changes are near the same horizontal location on all observed isopycnals, as if the inshore water results from a northward flow at all depths. Some of the most striking spice signals are seen on Line 93, perhaps because it is closer to the southern source for warm-salty anomalies. An eddy was observed in the winter of 2006 with edges so sharp that they were comparable to the glider's horizontal resolution of about 3 km (seen at 210 and 260 km in Fig. 10c). Across this eddy, the potential temperature change on the 26 kg m$^{-3}$ isopycnal approaches 2°C. This eddy also separates an inshore region of relatively strong spice variability from a more quiescent offshore region.

## Biophysical interactions

Phytoplankton and primary production are central to understanding the food web consequences of climate variability on the ecosystem. Physical processes affect phytoplankton through turbulent fluxes of nutrients, the interaction of solar radiation and vertical advection, and currents that mix and transport plankton. Analysis of glider-based measurements of Chl *a* fluorescence, as estimates of phytoplankton variations, must consider these physical influences, grazing, and nonphotochemical quenching that affects the relation between phytoplankton abundance and fluorescence. In situ measurements of fluorescence from phytoplankton Chl *a* include diel variations attributable to quenching and to the diel cycle

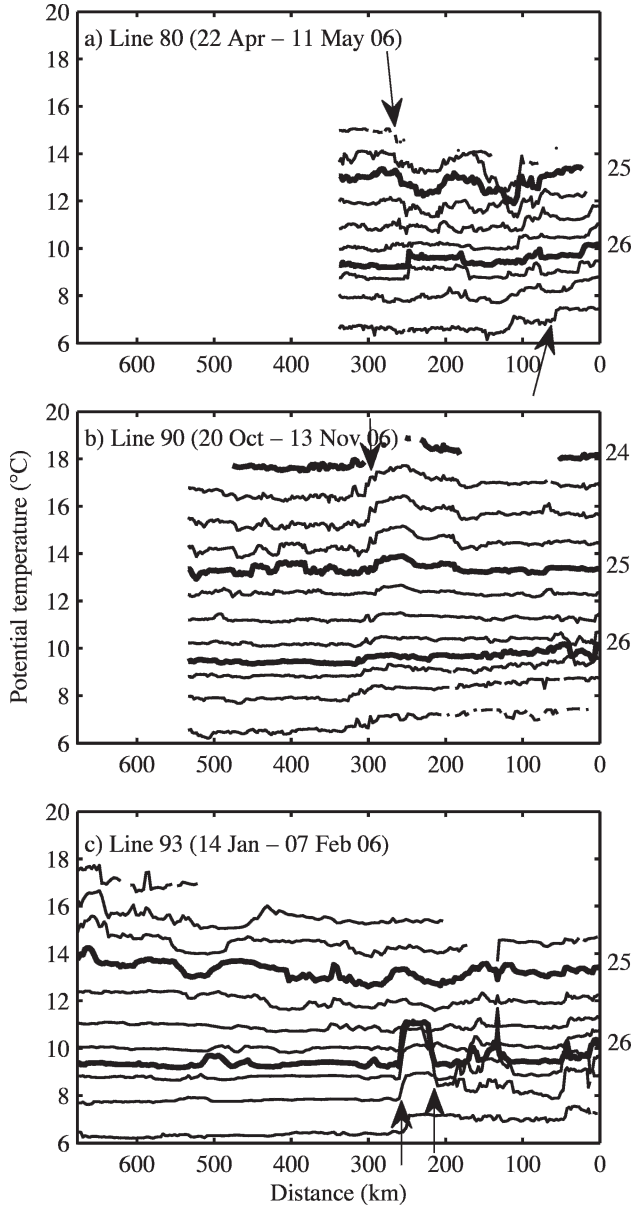


Fig. 10. Potential temperature on isopycnals as a measure of spice along (a) Line 80 from 22 Apr to 11 May 2006, (b) Line 90 from 20 Oct to 13 Nov 2006, and (c) Line 93 from 14 Jan 2006 to 07 Feb 2006. Distance is measured along the glider track from the most inshore profile. Potential temperature is plotted on isopycnals separated by 0.25 kg $m^{-3}$. The $\sigma_\theta$ = 24, 25, and 26 lines are thick. Arrows indicate spice fronts that span significant ranges of density and are discussed in the text.

of grazing. Diel periodicity of phytoplankton quenching is apparent in the mixed layer in Figs. 6 and 7, where a diminution in Chl *a* fluorescence recurs every 24 h, typically centered near local noon. Here we discuss biophysical interactions seen in our data.

*Mesoscale variability of Chl* a—Phytoplankton are notoriously patchy with probability distributions closer to lognormal than Gaussian. To explore the scales of Chl *a*, structure functions of the logarithm of fluorescence are shown in Fig. 11. The logarithm is appropriate to the probability distribution and accentuates small-scale features embedded in large-scale changes of Chl *a* intensity, such as those seen in the autumn offshore variations of Fig. 7. As with *S*, the Chl *a* variability on levels is dominated by the largest well-measured scales near 200 km and is greater in spring than fall. The clipped sawtooth pattern in the structure functions on shallow levels describes the diel cycle of fluorescence quenching. The 20-m vertical decay scale of quenching seen in Fig. 11 is typical in our data of waters enriched in Chl *a*; quenching penetrates to 60 m in optically clearer waters offshore.

On all but the deepest isopycnals in Fig. 11, the variability of Chl *a* is an order of magnitude less than on levels, even at the shortest separations where one might have anticipated differences to result mainly from instrumental noise. This quantifies how well shallow Chl *a* behaves like a passive tracer. On deeper levels, variability is not reduced on isopycnals, indicating that deep chlorophyll has fundamentally different dynamics than shallow chlorophyll. Like those of salinity, the structure functions on shallow density surfaces plateau at scales of 50–100-km separation, suggesting that much of the isopycnal structure is related to mesoscale stirring. Also like *S*, this variability on $\sigma_\theta$ surfaces is greatest in autumn, perhaps indicating when mesoscale stirring is most effective. The differences between levels and isopycnals and between seasons and the emergence of a dominant mesoscale on isopycnals when none exists on levels are all similar between Chl *a* and salinity, suggesting parallels between the mechanisms by which shallow variability in the two properties is created.

The fact that chlorophyll variability below the seasonal thermocline is not reduced on isopycnals the way salinity and shallow chlorophyll variability are suggests a unique mechanism for creating deep chlorophyll variability. Figure 12, which shows the same subthermocline feature seen at 230 km in Fig. 10c, describes one mechanism by which deeper Chl *a* variability and spice variability are generated. Although the salinity feature gives the appearance of having pushed up from the salty water below, its effect on density is almost perfectly compensated by temperature, suggesting that it results from horizontal motions. This compensation can be seen in Fig. 12 from how isopycnals and isohalines are nearly orthogonal at the edges of the intrusion.

Although it is below the euphotic zone, the water in this feature has a clear fluorescence signature, indicating that it was in mixing contact with the surface more recently than the surrounding water. The salinity and chlorophyll fronts that define the edges of the feature coincide precisely. This pattern likely arose when warm and salty higher-chlorophyll water was advected into close proximity with cooler, fresher water that was also lower in chlorophyll; it is noteworthy that the inshore edge of the intrusion coincides with a strong southward jet in vertically averaged current velocity. The co-occurrence of salinity and chlorophyll gradients is understood as the behavior of two stirred passive tracers (Hodges and Rudnick 2006).

The structure functions in Fig. 11 show that much of chlorophyll variability is produced by vertical advection of

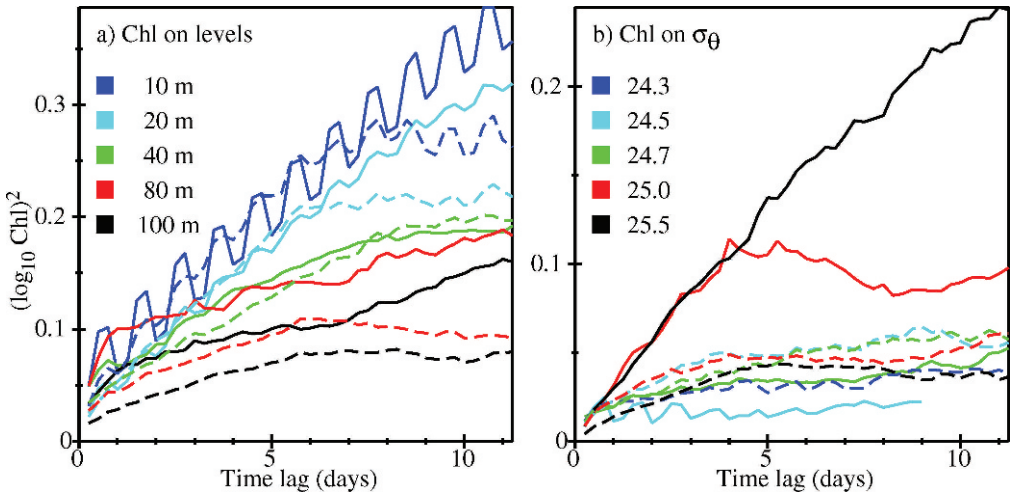


Fig. 11. Structure functions of $\log_{10}$ Chl *a* fluorescence sorted by time separation. (a) Differences between samples at the same depths of 10, 20, 40, 80, and 100 m. (b) Differences between values on the same potential density surfaces of 24.3, 24.5, 24.7, 25.0, and 25.5. Data are from Line 80 (solid line) and Lines 90 and 93 (dashed). Variability is greatly reduced on the shallow isopycnals. On the 25 and 25.5 isopycnals, below the seasonal thermocline, however, it is comparable on levels and isopycnals, suggesting different dynamics.

distributions that are much smoother on $\sigma_\theta$ surfaces. There remain, however, variations of Chl *a* on isopycnals because chlorophyll is not a strictly passive tracer. Uplifting an isopycnal increases the light level on it and can stimulate phytoplankton growth if there are adequate nutrients; this response may be enhanced by along-isopycnal upwelling (e.g., Ryan et al. 1999). The relationship between chlorophyll concentration and isopycnal displacements was investigated using as a measure of isopycnal displacement the potential density anomaly $\sigma' = \sigma - <\sigma>$, where $\sigma$ is the potential density and $<\sigma>$ is the local mean density computed as the average at the same depth over all profiles made within 6 d. Consequently, the $\sigma'$ anomalies have scales of less than 6 d or 150 km and, like the displacement of an isopycnal, describes vertical excursion. Rather than the change in depth of a given density surface, $\sigma'$ describes the change in density at a given depth.

The DCM is a ubiquitous feature of tropical and subtropical ocean ecosystems (Venrick et al. 1973), and chlorophyll concentrations are often several times greater in the DCM than above or below. To examine chlorophyll variability at the DCM, we define $F$ as the maximum Chl *a* fluorescence in a profile (i.e., at the chlorophyll maximum), take $<F>$ as the local mean of chlorophyll at the same depth averaged over ±6 d, and use the ratio $F/<F>$ as an

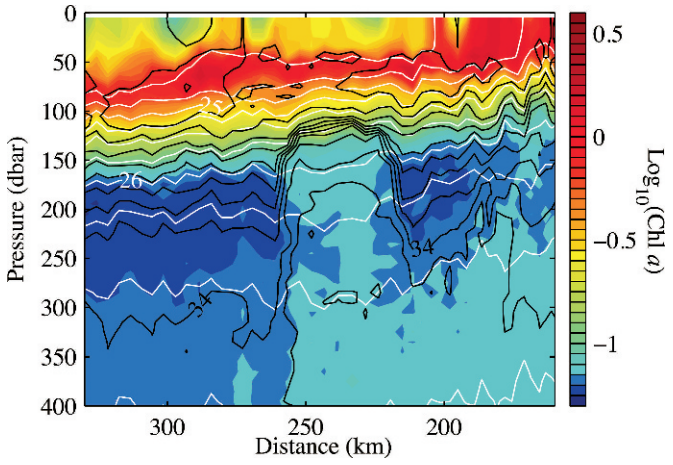


Fig. 12. Salinity contours (black) plotted over chlorophyll fluorescence for the Line 93 density-compensated intrusion pictured in Fig. 10c. Potential density contours are plotted in white. Contour spacing is 0.1 for salinity and 0.25 for $\sigma_\theta$. Chlorophyll is displayed on a logarithmic scale to emphasize the small concentrations below the DCM.

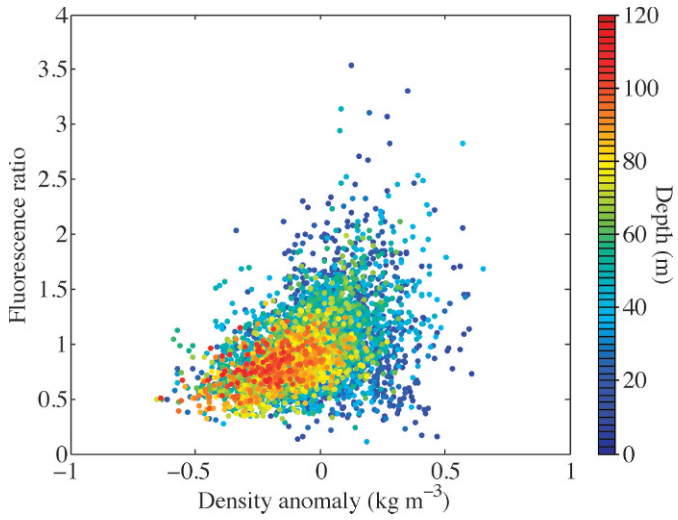


Fig. 13. Relation of (quenching corrected) Chl *a* fluorescence enhancement $F$ at the chlorophyll maximum vs. potential density anomaly for gliders on all three CalCOFI lines. Positive density anomalies, marking water that has been uplifted, are associated with locally enhanced fluorescence. Color indicates the depth of the DCM in meters; the effect of uplifting appears to be magnified at shallow depths.

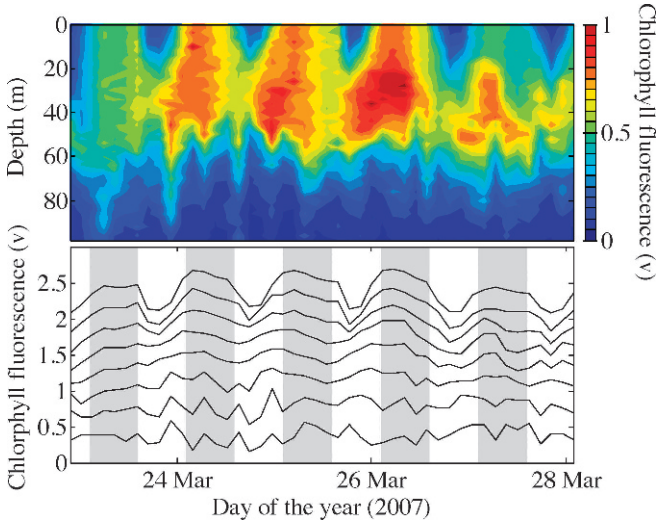


Fig. 14. Example of the diel cycle of Chl *a* from the spring of 2007 on Line 80. (a) Raw Chl *a* fluorescence. (b) The same data averaged vertically into 8-m bins centered on depths from 4 to 60 m in 8-m steps. Gray shading indicates night. The vertical axis is fluorescence (v). Near the surface (4–20 m), fluorescence is diurnal with a minimum near midday. From 28 to 44 m, it is diurnal with a minimum near dawn, suggesting a phytoplankton growth cycle. Below 50 m there is little evidence of a diel cycle.

indication of the local enhancement of Chl *a*. (For $F$, we actually use the quenching-corrected fluorescence, as described later.) Figure 13 is a scatter plot of $F/\langle F \rangle$ against the density anomaly at the chlorophyll maximum from dives on all three glider lines; each point represents the chlorophyll and density on one of 7112 profiles. If chlorophyll were a passive tracer, neither chlorophyll nor the chlorophyll maximum would be related to the density anomaly. The plot shows that positive density anomalies, which represent upward water displacements, are associated with locally increased fluorescence, consistent with irradiance-stimulated phytoplankton growth.

*Diel variability and fluorescence quenching*—Figure 14 shows a 5-d *Spray* record of upper-ocean Chl *a* fluorescence from a March 2007 deployment on Line 80. Most obvious is the diel cycle on shallow levels. One might assume that this was the effect of nonphotochemical fluorescence quenching (e.g., Kiefer 1973) when intense light reduces the fluorescence yield per cell. However, not all fluorescence daily periodicity is the result of quenching. Light can stimulate cyclic growth, and grazing, with its own diel cycle, can produce true changes in chlorophyll concentration. This is seen in Fig. 14, where near the surface (4–20 m) fluorescence is a minimum at midday, when quenching is strongest, while a little deeper in the water column (28–44 m), fluorescence is usually smallest at dawn and increases to a maximum at dusk, consistent with

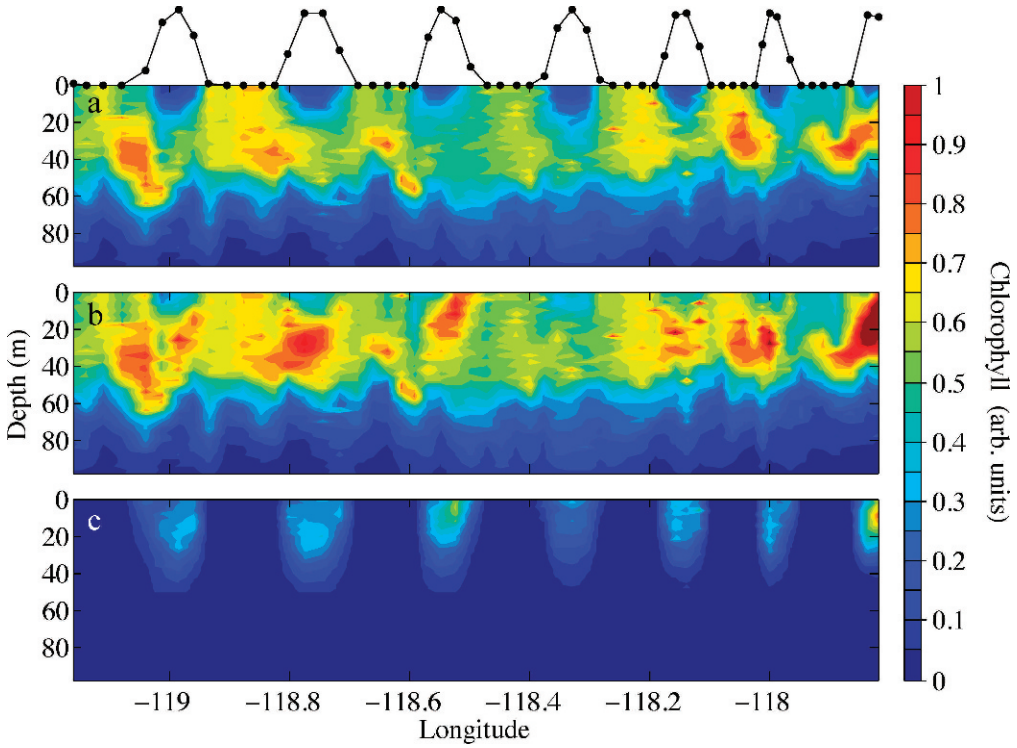


Fig. 15. A week of Chl *a* fluorescence data from the spring of 2006 along Line 93. (a) Raw fluorescence converted to chlorophyll concentration, (b) the same section after correction for nonphotochemical quenching, and (c) the correction. The black line at the top shows relative light intensity based on the position of the sun. Black dots locate each dive.

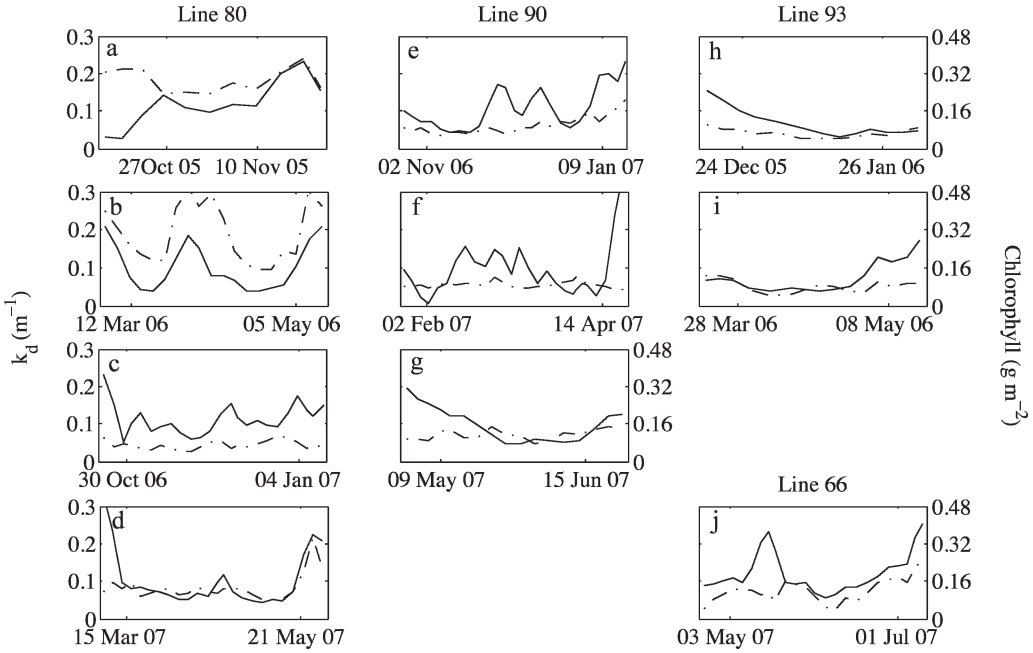


Fig. 16. Inferred diffuse attenuation coefficient, $k_d$ (solid), and chlorophyll concentration vertically integrated over the upper 200 m (dash-dot), averaged into 4-d bins and plotted vs. time. (a–d) Line 80 deployments, (e–g) Line 90 deployments, and (h–j) Line 90 and Line 66 (off Monterey) deployments. Note the resemblance between $k_d$ and integrated fluorescence.

biomass accumulation during the daylight hours and loss during the night. Deeper still, the diel signal disappears.

A method of identifying the variability of Chl *a* fluorescence caused by photoquenching has been developed to permit the study of other signals in the upper ocean. Fluorescence is the only optical property measured, so estimating the degree of quenching is a delicate problem. We make the following assumptions. (1) Aside from the effect of quenching, fluorometer output is linearly proportional to chlorophyll concentration—this is supported by laboratory calibrations. (2) The degree of quenching per cell depends only on irradiance and not, for example, on such factors as bulk chlorophyll concentration or the history of insolation. (3) The quenching response of Chl *a* is effectively instantaneous—in fact, it is short compared to a day (e.g., Krause and Weis 1991) so that observed fluorescence quenching is in phase with the daylight cycle (black line in Fig. 15). Neglecting additional sources of error such as chlorophyll "packaging" or self-shading and calibration uncertainty, these assumptions suggest a simple relationship between $F$, the chlorophyll concentration measured by fluorescence, and true chlorophyll concentration, $C$:

$$F(\mathbf{x},t) = q[\varphi(\mathbf{x},t)]C(\mathbf{x},t),$$

where $q$ is a quenching function that depends only on irradiance, $\phi$; $F$ is measured along the glider's path, and $\phi$ is estimated from the downward clear-sky irradiance at the surface (neglecting clouds and sea state) and the transmission coefficient of the air–sea interface.

The unknown rate of decay of light intensity with depth is inferred from the observed depth decay of the covariance of fluorescence and the estimated surface irradiance. To do this, the record is broken into 4-d overlapping chunks, and the covariance of surface irradiance and fluorescence is computed for each chunk in 2-m-depth bins. A diffuse attenuation coefficient, $k_d$, is determined for each chunk by fitting the function $\exp(k_d Z)$ to the covariance estimates, neglecting any vertical variation of $k_d$.

Beam attenuation coefficient and chlorophyll fluorescence are often strongly correlated in the ocean (e.g., Behrenfeld and Boss 2006): light attenuates more rapidly in high-chlorophyll water. Although nonfluorescent particles and dissolved substances contribute to light attenuation, it is not surprising that variations in our estimates of $k_d$ are broadly similar to those in vertically integrated chlorophyll concentration (Fig. 16). Both the attenuation coefficient and the integrated chlorophyll are generally larger over the continental shelf than in the deep ocean.

Having measured $F$ and estimated $\phi$, it remains to determine $q$. We assume it has the form

$$q = \frac{k}{k + \varphi},$$

where $k$ is a constant. This form is chosen as the simplest with the following properties: for $\varphi = 0$ (darkness), $q = 1$, so there is no quenching and $F = C$; as light intensity increases, $q$ decreases, approaching zero. The best $k$ is taken as the one that makes the depth-averaged covariance of $C$ and $\varphi$ weighted by $\exp(k_d Z)$ vanish (so $C$ and irradiance are uncorrelated on average). This arbitrary weighting emphasizes correcting fluorescence quenching near the surface, where it is strongest. While $k$ is held constant within each deployment, it is recomputed for each

deployment. With $\varphi$ nondimensionalized to reach a maximum value of unity just above the sea surface with the sun directly overhead, the values obtained for $k$ across most deployments are in the range of 0.2–0.3. Dividing $F$ by $q$, we obtain $C$, the estimated true chlorophyll concentration.

*Temporal evolution in a water parcel*—Gliders alone are unable to deal with many of the most complex and important questions about ecosystem interactions, but they can continue to be very useful when working in concert with other observations. In an example of this, we employed a *Spray* to follow the temporal evolution of an apparently homogeneous water parcel marked by a satellite-tracked drifter drogued at 15 m. Drifter positions every 10 min were transmitted every 30 min to a shore-based glider pilot who navigated the glider alternately along the axis of drifter motion and then across that axis (Fig. 17a). The $T$ and $S$ panels of that figure illustrate how physical conditions in the upper 30–40 m remained relatively constant over this 3-d tracking experiment, suggesting that the drifter successfully stayed within the same water parcel. Deeper strata show variations influenced by internal waves but no significant change over time.

Acoustic backscatter showed distinct, reproducible patterns of nighttime surface enrichment (Fig. 17e—ABS). In daytime, scatterers descended below the 150-m depth sampled on these dives. Near-surface Chl *a* (Fig. 17d—Chl) shows a reproducible diel cycle with a minimum around 10:00 h local time and a progressive increase at all times of day over the 3 d. Because these measurements sample a region around the drifter and spatial variation of physical characteristics is small, we interpret this day-to-day temporal variation as in situ phytoplankton growth. Assuming a linear fluorescence vs. chlorophyll relation, this change corresponds to a 48% increase in Chl *a* concentration in the upper 25 m, or a net specific phytoplankton growth rate of 0.20 $d^{-1}$. This in situ estimate of net growth compares well with in situ incubation measurements on successive 24-h periods over the same period, which showed an average specific Chl *a* growth rate of 0.18 $d^{-1}$ (range: 0.16–0.22 $d^{-1}$, five depths in the upper 25 m; M. Landry pers. comm.).

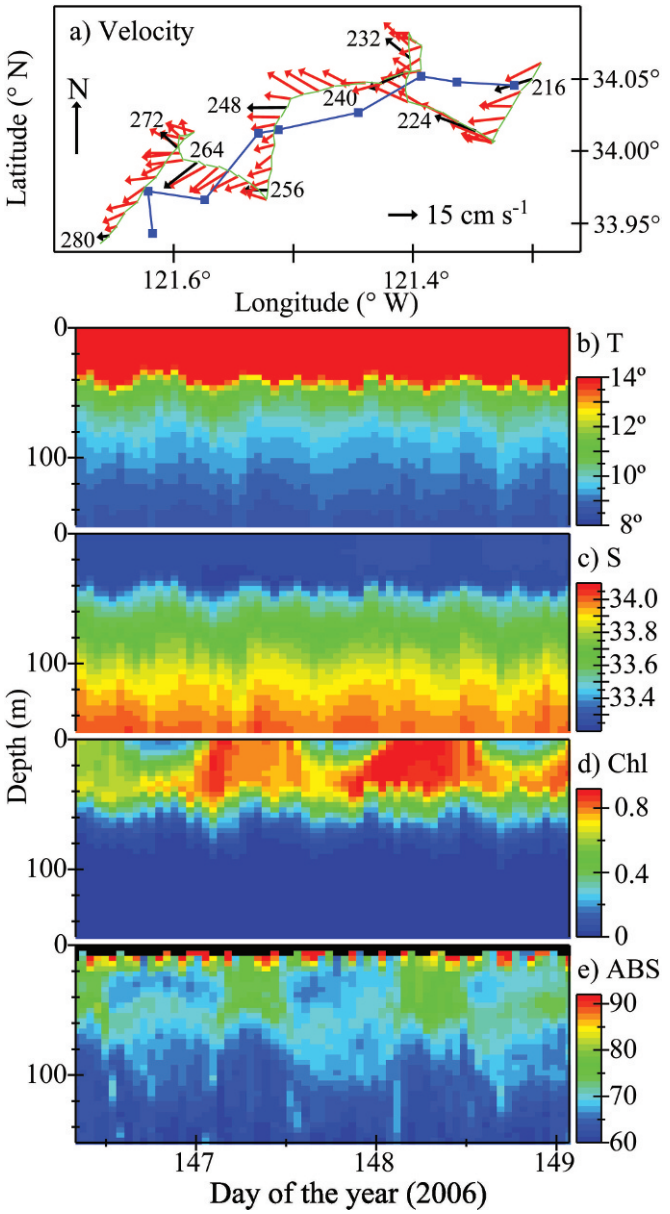


Fig. 17. (a) The depth-averaged velocity (0–150 m) from a *Spray* glider (vectors) tracking a Globalstar drifter in May 2006. Every eighth dive is enumerated, and its velocity is plotted in black. Drifter positions simultaneous to these dives are plotted as blue squares. Glider sections from the same time period are of (b) temperature, (c) salinity, (d) Chl *a*, (e) 750-kHz backscatter, and (f) $\sigma_\theta$.

## Discussion

Because gliders move slowly, they make feasible sustained ocean observations of high spatial resolution in the upper ocean. We have begun such measurements in the southern CCS with an eye toward the connection of physical and biological variability, particularly on seasonal and longer time scales. The observational record is not yet long enough to provide accurate pictures of typical seasonally varying structures and relations, but the high resolution of the observations makes possible the diverse set of studies and hypotheses presented here.

On the physical side, many general circulation features and seasonal structures are consistent with more statistically reliable results based on lower-resolution CalCOFI data: the salty Inshore Countercurrent and the fresher equatorward nearshore upwelling-driven circulation are prominent, the former prominent in fall–winter and the latter strongest in spring–summer; pycnocline slope and equatorward geostrophic shear are weak in fall; eddies are prominent in both seasons and have scales of O (100 km); and the signature of the California Current is shallow and filamentous. Noteworthy findings include (1) a second poleward undercurrent 200 km offshore that is evident only with absolute current measurements, (2) a mesoscale

eddy near Pt. Conception that persisted in one location for at least 2 months and either persisted for 6 months or recurred at the same position, (3) numerous secondary density fronts in the upper ocean offshore of the main pycnocline front (when one exists) that are found throughout the year but are more organized in spring–summer, and (4) that once the effect of vertical displacement is removed by looking at distributions on potential density surfaces, the variability of Chl *a* and of spice are similarly concentrated in the mesoscale and are stronger in spring than fall.

The offshore poleward undercurrent may be a concentration of the California Undercurrent that Lynn and Simpson (1990), using lower-resolution measurements, show extends well offshore. While the water properties of the California Current are evident, the offshore pycnocline slope is small, and the measured depth-averaged current shows offshore flow below 200 m to be mostly poleward; this could be an interannual effect since the equatorial Pacific exhibited a weak El Niño in 2006. If, however, absolute velocities below 200 m are generally poleward, this would help explain how some zooplankton species avoid being flushed out of the CCS by growing in equatorward-flowing surface waters and then entering dormancy in poleward-flowing subsurface waters to return (e.g., Johnson 2007). In any case, we believe that the evidence now available makes it clear that absolute velocity measurements and mesoscale resolution (25 km) are necessary to unravel the complexities of the CCS.

Our initial *Spray*-based measurements in the CCS reveal a close association between horizontal fronts in physical and biological properties, including seawater density, phytoplankton Chl *a*, and acoustic backscatter at 750 kHz. Although the biophysical importance of frontal features is not surprising (e.g., Franks 1997), the gliders enable us to resolve the subsurface and horizontal structure of such fronts and their persistence in time in a way that is impractical from ships or other in situ measurements. The fronts are a major source of spatial structure in the water column that apparently mark concurrent abrupt changes of phytoplankton and mesozooplankton, including, in many cases, changes in their vertical distributions. Although we are not able to resolve compositional differences in the plankton with our glider-based sensors, parallel shipboard investigations in our study site will reveal whether dominant species and growth and grazing rates also change across these frontal features.

These sharp spatial gradients are likely to be of considerable significance for a variety of mobile predators that can select their spatial habitats, including planktivorous fishes (Logerwell and Smith 2001), seabirds (Sydeman et al. 2006), and marine mammals (Tynan et al. 2005). To the extent that such predators can locate and remain in gradient regions of enhanced prey abundance, these fronts gain importance as likely sites of increased foraging success and predator growth rates. Our results suggest that there may be seasonal modulation of the spatial variability attributable to these frontal features. The spring–summer time period appears to have stronger, more reproducible fronts, while the late fall–early winter appears to show less spatial variation on large scales and mesoscales. If this pattern is substantiated, it suggests that seasonal changes in spatial structure, as much as seasonal variations in prey abundance, may be key determinants of predator population growth.

On a smaller spatial scale, the association of vertical movements of phytoplankton Chl *a* with vertical displacements of isopycnal surfaces is striking. Although the covariability of phytoplankton with internal waves and other density variations is well known (e.g., Lennert-Cody and Franks 2002), repeated glider observations over a large area establish this interrelationship particularly clearly. In the case of one section in October 2005, the pronounced tidally synchronized vertical displacements of isopycnal surfaces underscores the importance of internal tidal waves in altering the light environment and potentially the growth rate of the entrained phytoplankton cells. Because Chl *a* is advected by many vertical motions, its variability on potential density surfaces is dramatically smaller than it is at fixed depths. More revealing, spice and Chl *a* on isopycnals are dominated by the mesoscale, even though on levels they are dominated by large scales. This suggests that mesoscale variability is the source of the structure in both these quasi-passive variables.

The interpretation of acoustic backscatter at a single frequency is complicated by several factors (e.g., Holliday and Pieper 1995; Foote and Stanton 2000). Based on the sound frequency (750 kHz), the steepness of the usual particle size spectrum, and the relatively small (ca. 10 $m^3$) sampled volume in the operating range from 11 to 20 m from the source, it is likely that most of the acoustic backscatter is attributable to mesozooplankton and micronekton organisms rather than larger, rarer adult fish and other nekton. We note that the marked spatial changes in intensity of acoustic backscatter that we have observed do not necessarily imply changes in zooplankton biomass, as differences in body size, species composition, elastic properties of the animals, or orientation can also markedly influence acoustic target strength returned (Stanton et al. 1998; De Robertis 2001). However, in our study site, Lynn (2003) previously established a strong correlation between volume backscatter from a ship-mounted ADCP and net-collected zooplankton biomass.

In conclusion, autonomous ocean gliders have substantially improved our ability to resolve ocean phenomena in the CCS on several different spatial scales and to do so at a fraction of the cost associated with comparable shipboard measurements. The direct and indirect effects of movements of isopycnal surfaces on phytoplankton, close alignment of physical and biological properties at frontal boundaries, and covariation of biophysical features, including eddies and spice anomalies, underscore the importance of high-resolution in situ measurements over relatively broad geographic distances. As *Spray* gliders can now be deployed reliably for extended periods, we look forward to resolving seasonal and climate-scale temporal changes in the interactions between such physical and biological features and their underlying dynamical causes.

## References


Behrenfeld, M. J., and E. Boss. 2006. Beam attenuation and chlorophyll concentration as alternative optical indices of phytoplankton biomass. J. Mar. Res. **64:** 431–451.

Checkley, D. M., Jr., R. C. Dotson, and D. A. Griffith. 2000. Continuous, underway sampling of eggs of Pacific sardine (*Sardinops sagax*) and northern anchovy (*Engraulis mordax*) in spring 1996 and 1997 off southern and central California. Deep-Sea Res. II **47:** 1139–1155.

Chelton, D. B., and R. E. Davis. 1982. Monthly mean sea-level variability along the west coast of North America. J. Phys. Oceanogr. **12:** 757–784.

Chereskin, T. K., and M. Trunnel. 1996. Correlation scales, objective analysis, and absolute geostrophic flow in the California Current. J. Geophys. Res. **101:** 22,619–22,629.

———, and others. 2000. Spatial and temporal characteristics of the mesoscale circulation of the California Current from eddy-resolving moored and shipboard measurements. J. Geophys. Res. **105:** 1245–1269.

Collins, C. A., N. Garfield, T. A. Rago, F. W. Rischmiller, and E. Carter. 2000. Mean structure of the inshore countercurrent and California undercurrent off Point Sur, California. Deep-Sea Res. II **47:** 765–782.

Davis, R. E. 1985. Drifter observations of coastal surface currents during CODE: The method and descriptive view. J. Geophys. Res. **90:** 4741–4755.

———, C. E. Eriksen, and C. P. Jones. 2002. Autonomous buoyancy-driven underwater gliders, p. 37–58. *In* G. Griffiths [ed.], The technology and applications of autonomous underwater vehicles. Taylor and Francis.

Derobertis, A. 2001. Validation of acoustic echo counting for studies of zooplankton behavior. ICES J. Mar. Sci. **58:** 543–561.

Flament, P. 2002. A state variable for characterizing water masses and their diffusive stability: Spiciness. Prog. Oceanogr. **54:** 493–501.

Foote, K. G., and T. K. Stanton. 2000. Acoustical methods, p. 224–258. *In* R. P. Harris, P. H. Wiebe, J. Lenz, H. R. Skoldal and M. Huntley [eds.], ICES zooplankton methodology manual. Academic.

Franks, P. J. S. 1997. New models for the exploration of biological processes at fronts. ICES J. Mar. Sci. **54:** 161–167.

Hayward, T. L., and A. W. Mantyla. 1990. Physical, chemical and biological structure of a coastal eddy near Cape Mendicino. J. Mar. Res. **48:** 825–850.

Hickey, B. M. 1979. The California Current system: Hypothesis and facts. Prog. Oceanogr. **8:** 191–279.

Hodges, B. A., and D. L. Rudnick. 2006. Horizontal variability in chlorophyll fluorescence and potential temperature. Deep-Sea Res. I **53:** 1460–1482.

Holliday, D. V., and R. E. Pieper. 1995. Bioacoustical oceanography at high frequencies. ICES J. Mar. Sci. **52:** 279–296.

Jackett, D. R., and T. J. McDougall. 1985. An oceanographic variable for the characterization of intrusions and water masses. Deep-Sea Res. **32:** 1195–1207.

Johnson, C. L. 2007. Retention of dormant copepods in deep basins of the Southern California Bight. Mar. Ecol. Prog. Ser. **336:** 203–210.

Johnson, G. C., J. M. Toole, and N. G. Larson. 2007. Sensor corrections for Sea-Bird SBE-41CP and SBE-41 CTDs. J. Atmos. Oceanic Tech. **24:** 1117–1130.

Kelly, K. A., R. C. Beardsley, R. Limeburner, K. H. Brink, J. D. Paduan, and T. K. Chereskin. 1998. Variability of the near-surface eddy kinetic energy in the California Current based on altimetric, drifter, and moored current data. J. Geophys. Res. **103:** 13067–13084.

Kiefer, D. A. 1973. Fluorescence properties of natural phytoplankton populations. Mar. Biol. **22:** 263–269.

Kim, H.-K., and A. J. Miller. 2007. Did the thermocline deepen in the California Current after the 1976/77 climate regime shift? J. Phys. Oceanogr. **37:** 1733–1739.

Krause, G. H., and E. Weis. 1991. Chlorophyll fluorescence and photosynthesis: The basics. Annu. Rev. Plant Physiol. Plant Mol. Biol. **42:** 313–349.

Kolmogorov, A. N. 1941. The local structure of turbulence in incompressible viscous fluids for very large Reynolds numbers. C.C. Acad. Sci. U.R.S.S. **30:** 299–303.

Lavaniegos, B. E., and M. D. Ohman. 2007. Coherence of long-term variations of zooplankton in two sectors of the California Current System. Prog. Oceanogr. **75:** 42–69.

Lennert-Cody, C. E., and P. J. S. Franks. 2002. Fluorescence patches in high-frequency internal waves. Mar. Ecol. Prog. Ser. **235:** 29–42.

Logerwell, E. A., and P. E. Smith. 2001. Mesoscale eddies and survival of late-stage Pacific sardine (*Sardinops sagax*) larvae. Fish. Oceanogr. **10:** 13–25.

Lynn, R. J. 2003. Variability in the spawning habitat of Pacific sardine (*Sardinops sagax*) off southern and central California. Fish. Oceanogr. **12:** 541–553.

———, and S. J. Bograd. 2002. Dynamic evolution of the 1997–1999 El Niño-La Niña cycle in the southern California Current System. Prog. Oceanogr. **54:** 59–75.

———, ———, T. K. Chereskin, and A. Huyer. 2003. Seasonal renewal of the California Current: The spring transition off California. J. Geophys. Res. **108:** 3279. doi:10.1029/2003JC001787.

———, and J. J. Simpson. 1987. The California Current system: The seasonal variability and its physical characteristics. J. Geophys. Res. **92:** 12947–12966.

———, and ———. 1990. The flow of the undercurrent over the continental borderland off southern California. J. Geophys. Res. **95:** 12995–13008.

Mantua, N. J., S. R. Hare, Y. Zhang, J. M. Wallace, and R. C. Francis. 1997. A Pacific interdecadal climate oscillation with impacts on salmon production. Bull. Am. Meteorol. Soc. **78:** 1069–1079.

McDougall, T. J. 1987. Neutral surfaces. J. Phys. Oceanogr. **17:** 1950–1964.

Munk, W. 1981. Internal waves and small-scale processes, p. 264–291. *In* B. A. Warren and C. Wunsch [eds.], Evolution of physical oceanography. MIT Press.

Ohman, M. D., and E. L. Venrick. 2003. CalCOFI in a changing ocean. Oceanography **16:** 76–85.

Ramp, S. R., J. L. McLean, C. A. Collins, C. S. Semtner, and A. J. Hays. 1997. Observations and modeling of the 1991–1992 El Niño signal off central California. J. Geophys. Res. **102:** 5553–5582.

Roemmich, D., and J. A. McGowan. 1995. Climatic warming and the decline of zooplankton in the California Current. Science **267:** 1324–1326.

Rudnick, D. L., R. E. Davis, C. C. Eriksen, D. Fratantoni, and M. J. Perry. 2004. Undersea gliders for ocean research. J. Mar. Tech. Soc. **38:** 73–84.

Ryan, J. P., J. A. Yoder, J. A. Barth, and P. C. Cornillion. 1999. Chlorophyll enhancement and mixing associated with meanders of the shelf break front in the Mid-Atlantic Bight. J. Geophys. Res. **104:** 23479–23494.

Saunders, M. W., and G. A. McFarlane. 1997. Observations on the spawning distribution and biology of offshore Pacific hake (*Merluccius productus*). CalCOFI Rep. **38:** 147–157.

Sherman, J., R. E. Davis, W. B. Owens, and J. Valdes. 2001. The autonomous underwater glider "Spray." IEEE Oceanic Eng. **26:** 437–446.

Smith, S. L., B. H. Jones, L. P. Atkinson, and K. H. Brink. 1986. Zooplankton in the upwelling fronts off Pt. Conception, California, p. 195–213. *In* J. C. J. Nihoul [ed.], Marine interfaces ecohydrodynamics. Elsevier Oceanography Series, 42.

Stanton, T. K., D. Chu, P. H. Wiebe, L. V. Martin, and R. L. Eastwood. 1998. Sound scattering by several zooplankton groups. I. Experimental determination of dominant scattering mechanisms. J. Acoust. Soc. Am. **103:** 225–235.

Sydeman, W. J., and others. 2006. Planktivorous auklet *Ptychoramphus aleuticus* responses to ocean climate, 2005: Unusual atmospheric blocking? Geophys. Res. Lett. **33:** L22S09, doi: 10.1029/2006GL026736.

Tynan, C. T., D. G. Ainley, J. A. Barth, T. J. Cowles, S. D. Pierce, and L. B. Spear. 2005. Cetacean distributions relative to ocean processes in the northern California Current System. Deep-Sea Res. II **52:** 145–167.

Venrick, E. L., J. A. McGowan, and A. W. Mantyla. 1973. Deep maxima of photosynthetic chlorophyll in the Pacific Ocean. Fish. Bull. (US) **71:** 41–52.

Veronis, G. 1972. On properties of seawater defined by temperature, salinity, and pressure. J. Mar. Res. **30:** 227–255.

*Received: 24 September 2007*
*Accepted: 18 April 2008*
*Amended: 21 May 2008*